Quantifying the impact of bedrock topography uncertainty on 100-year Pine Island Glacier projections

Andreas Wernecke[1,1], Tamsin Edwards[2,2], Philip B. Holden[3,3], Neil Robert Edwards[4,4], and Stephen L Cornford[5,5]

[1]Max Planck Institute for Meteorology
[2]King's College London
[3]Open University
[4]The Open University
[5]Swansea University

November 30, 2022

Abstract

The predicted Antarctic contribution to global-mean sea-level rise is one of the most uncertain among all major sources. Partly this is because of instability mechanisms of the ice flow over deep basins. Errors in bedrock topography can substantially impact the projected resilience of glaciers against such instabilities. Here we analyze the Pine Island Glacier topography to derive a statistical model representation. Our model allows for inhomogeneous and spatially dependent uncertainties and avoids unnecessary smoothing from spatial averaging or interpolation. A set of topography realizations is generated representing our best estimate of the topographic uncertainty in ice sheet model simulations. The bedrock uncertainty alone creates a 5% to 25% uncertainty in the predicted sea level rise contribution at year 2100, depending on friction law and climate forcing. Pine Island Glacier simulations on this new set are consistent with simulations on the BedMachine reference topography but diverge from Bedmap2 simulations.

Quantifying the impact of bedrock topography uncertainty in Pine Island Glacier projections for this century*

Andreas Wernecke[1,2,3], Tamsin L. Edwards[4], Philip B. Holden[1], Neil R. Edwards[1], Stephen L. Cornford [5]

[1]School of Environment, Earth and Ecosystem Sciences, The Open University, Milton Keynes, UK
[2]Max-Planck-Institute for Meteorology, Hamburg, Germany
[3]Universität Hamburg, Hamburg, Germany
[4]Kings Collage London, London, UK
[5]Faculty of Science and Engineering, Swansea University, Swansea, UK

Key Points:

- Uncertainty in topography estimates has a significant impact on predictions for all tested friction laws
- Simulations with BedMachine and statistically generated topographies are more sensitive to upper-end climate forcing than with Bedmap2
- Pine Island Glacier is likely to transition into a more unstable state late mid-century for upper-end climate forcing

---

*accepted author manuscript

Corresponding author: Andreas Wernecke, `andreas.wernecke@mpimet.mpg.de`

Abstract

The predicted Antarctic contribution to global-mean sea-level rise is one of the most uncertain among all major sources. Partly this is because of instability mechanisms of the ice flow over deep basins. Errors in bedrock topography can substantially impact the projected resilience of glaciers against such instabilities. Here we analyze the Pine Island Glacier topography to derive a statistical model representation. Our model allows for inhomogeneous and spatially dependent uncertainties and avoids unnecessary smoothing from spatial averaging or interpolation. A set of topography realizations is generated representing our best estimate of the topographic uncertainty in ice sheet model simulations. The bedrock uncertainty alone creates a 5% to 25% uncertainty in the predicted sea level rise contribution at year 2100, depending on friction law and climate forcing. Pine Island Glacier simulations on this new set are consistent with simulations on the BedMachine reference topography but diverge from Bedmap2 simulations.

Plain Language Summary

We investigate the impact of uncertainties in the elevation of the bedrock underneath the ice of a particularly vulnerable glacier in Antarctica. We propose a new approach to better estimate how much future projections depend on knowledge of bedrock elevation. The main focus of this study is to represent the current understanding of the bedrock elevation as closely as possible so that our simulations accurately reflect the extent of our knowledge of the future glacier behaviour. In summary, we find that the mass of ice lost in simulations for year 2100, which contributes to the global mean sea level, can be affected by up to 25%. This highlights the value of closely-spaced bedrock measurement and of careful consideration of related uncertainties in ice-sheet simulations.

1 Introduction

The Antarctic ice sheet is one of the major sources of global sea level rise and is currently losing mass at a rate of 0.5 to 0.6 mm global mean Sea Level Equivalent per year (mm SLE a^{-1}), predominantly in the Amundsen Sea Embayment (ASE) area of the West Antarctic Ice Sheet (WAIS) (Shepherd et al., 2018; Bamber et al., 2018). The future response of the Antarctic ice sheet to a changing climate is one of the least well understood aspects of climate predictions (Oppenheimer et al., 2019).

Changes in the Antarctic ice sheet mass balance are largely governed by changes in the Surface Mass Balance (SMB) and ocean forcing via dynamical processes such as changing buttressing from ice shelves. Ice shelves, the floating extensions of grounded ice streams, can be weakened by elevated ocean or atmospheric temperatures and subsequent melt or collapse. Buttressing ice shelves have a stabilising effect on the ice sheet with the potential to suppress or delay Marine Ice Sheet Instability (MISI) (Schoof, 2007; Joughin & Alley, 2011). MISI can occur at ice sheets on retrograde topographies below sea level. Here a retreat of the Grounding Line (GL), the transition from grounded to floating ice, corresponds to a migration below thicker ice. For idealised conditions the mass flux across the GL increases rapidly with the ice thickness above it (Schoof, 2007). This additional mass loss can lead to an imbalance of the system causing a thinning of the ice upstream, which facilitates further GL retreat below even thicker ice. Large areas of the WAIS, including the ASE, lie on such retrograde topography (Fretwell et al., 2013). Pine Island Glacier (PIG), one of two major glacial systems of the ASE, has a large drainage basin and shares an ice divide with the Ronne-Filchner ice shelf drainage basin, so that a sustained thinning of PIG could ultimately influence most of the WAIS.

In the satellite record the ASE shows significant rates of thinning (Rignot et al., 2008; Mouginot et al., 2014; Shepherd et al., 2018), which have been linked to warm Circumpolar Deep Water entering the continental shelf (Dutrieux et al., 2014; Naughten et al., 2018; Rignot et al., 2014). Additional oceanic heat transport to the continent causes enhanced ocean melt which can thin and weaken the buttressing ice shelves. This might have caused a GL retreat and triggered Marine Ice Sheet Instability in the ASE at present (Joughin et al., 2014; Favier et al., 2014; Alley et al., 2015). Bamber and Dawson (2020) find a recent reduction of rates of mass loss from PIG even though it has maintained a negative mass balance and elevated flow speeds. This behaviour could be related to lower ocean temperatures in 2012-2013 compared with the 2000s (Milillo et al., 2017). In summary, PIG currently loses mass, shows strong sensitivity to ocean conditions and is situated on a bedrock topography which makes it vulnerable to instability.

Predictions of the dynamic ice sheet response are challenging because of poorly observed local ice properties and the bedrock underneath, including the bedrock elevation, which suffer from measurement and spatial interpolation errors. As described, MISI depends on the local topography; a regional sill along the GL can create a stable resting point for an otherwise unstable ice stream. This kind of topographic feature can be concealed even if the large-scale geometry is well represented, for example due to insufficient sampling density (Durand et al., 2011).

Several studies highlight the importance of the bedrock topography. Zhao et al. (2018) show that it influences the model inversion for basal traction coefficients. The impact of these results on forward simulations is, however, not investigated. The differences between Bedmap2 and its predecessor Bedmap1 can exceed the uncertainty in Antarctic sea level rise contribution from surface accumulation, melt rate, basal friction and ice viscosity combined (Schlegel et al., 2018). Consistent findings are reported by Nias et al. (2016, 2018). In order to investigate the impact of the topography uncertainty, random noise is imposed repeatedly on a reference topography in Sun et al. (2014) and Gasson et al. (2015). In 3000-year ice sheet simulations of the mid-Pliocene the sea level contribution can vary by more than 5 m global SLE (from 12.6 m to 17.9 m SLE) (Gasson et al., 2015). Sun et al. (2014) show with a similar approach that the sensitivity of modern ice sheet simulations to topographic uncertainty is much stronger for a longer correlation length (50 km) than for shorter values (5 to 10 km). This is despite equal noise amplitude and power spectral density which means that uncorrelated errors in the bedrock topography (e.g. from radar measurement noise) are less of a concern for ice sheet simulations than spatially correlated errors (e.g. from interpolation over large distances). Sun et al. (2014) also note that a topographic ridge near the PIG GL has a strong impact on the GL retreat if lowered or raised by only tens of metres but do not assess whether these kinds of larger spatial-scale errors in the topography are likely. Furthermore, the noise amplitude is solely based on the Bedmap2 uncertainty estimate so that the measurement locations are not directly taken into account.

We here move beyond randomised sensitivity studies to generate a statistical description of the current observational knowledge of the bedrock topography, creating an ensemble of representative topographies that are all consistent with these observations. We apply the ensemble to idealised but plausible forcing scenarios to quantify the uncertainty in sea level rise contribution predictions, arising from observational uncertainties in the PIG topography.

We introduce the airborne radar measurements used here and analyse the geostatistical properties in Section 2. Based on this we set up simulations of the ice sheet model BISICLES in Section 3. This includes the statistical generation of a set of bedrock topographies which are in agreement with observational constraints while aiming to fully represent their uncertainties. Section 3 further describes the initialisation and parameter inversion of the ice sheet model BISICLES, followed by a description of three friction laws and two climate forcings for the PIG simulations. Results are presented in Section 4 with focus on the sea level rise contribution uncertainty. Finally we discuss how bedrock uncertainty translates into predictive uncertainty in Section 5.

2 Data and Methods

We summarize our knowledge of the real bedrock in a multivariate random variable which is approximated by a Gaussian Process (GP). This statistical model can sample spatial fields of bedrock topography with local uncertainties and spatial covariance structure to represent measurement and interpolation uncertainties. To define a GP model, training data and covariance function parameters are required (Rasmussen & Williams, 2006). Ungridded airborne radar measurements are analysed to estimate the statistical characteristics of the bedrock topography observations. This provides us with the required GP model covariance function parameters. We train the GP to match observed values, given the observational uncertainty, and draw random samples to make the handling of topography uncertainty feasible for the ice sheet model BISICLES.

The airborne Radar Echo Sounding (RES) dataset used here is a union of two different collections, namely the one described in Holt, Blankenship, Morse, et al. (2006), and Operation Ice Bridge IRMCR2 Level-2 data from October 2009 to December 2017 (Paden et al., 2010). This combined collection consists of about 2.3 million ungridded radar measurements from the grounded PIG catchment area, as defined in Mouginot et al. (2017) based on Rignot et al. (2013). About 1.5% of these measurements are removed here by manual inspection due to inconsistencies (Text S1 and Figure S1 in the Supplement). For training the statistical model the RES dataset is sub-sampled for computational reasons. This is done by imposing a 2 km × 2 km grid onto the region and randomly selecting one measurement from each box from the combined measurement collection (giving about 25 000 measurements in total). This ensures a good spatial coverage while avoiding smoothing effects from averaging. The covariance function is derived from semivariograms on fully random subsets of 100 000 measurements without restriction on the proximity of sample points. Exponential functions are fitted to the semi-variance on scales of 25 km to 50 km to derive the uncorrelated uncertainty (σ_n^2), correlation length scale (ℓ) and far-field semivariance, or sill, (σ_c^2) to describe the spatial correlation characteristics. The uncorrelated uncertainty is an estimate of the uncertainty of two measurements at the same location and represents the measurement uncertainty, including uncertainties from sub-resolution variability, while a larger correlation length of the topography simplifies any interpolation and reduces the corresponding uncertainty. The far-field semivariance describes the amplitude of variations in the topography field. These exponential fits accurately capture the semi-variance (Figure S2 in the Supplement) which motivates our use of an exponential covariance function c_E for the GP, defined as:

$$COV(x_i, x_j) = c_E(r, \sigma_c^2, \ell, \sigma_n^2) = \sigma_c^2 \exp\Big(- \frac{r}{2\ell}\Big) + \sigma_n^2 \cdot \delta_{ij},$$

where $COV(x_i.x_j)$ is the covariance in the bedrock topography at the locations x_i and x_j, r is the physical distance between the locations x_i and x_j and δ_{ij} is the Kronecker delta which is one if $i = j$ and zero otherwise. The randomized sub-sampling for deriving the covariance parameters and the training data is repeated to capture the impact on the final simulations. See Text S2 in the Supplement for more information.

We generate random two-dimensional sample fields which adhere to the full spatial covariance matrix and the local observational uncertainties, as illustrated in Figure 1a. The topographic uncertainty increases with distance to the closest measure-

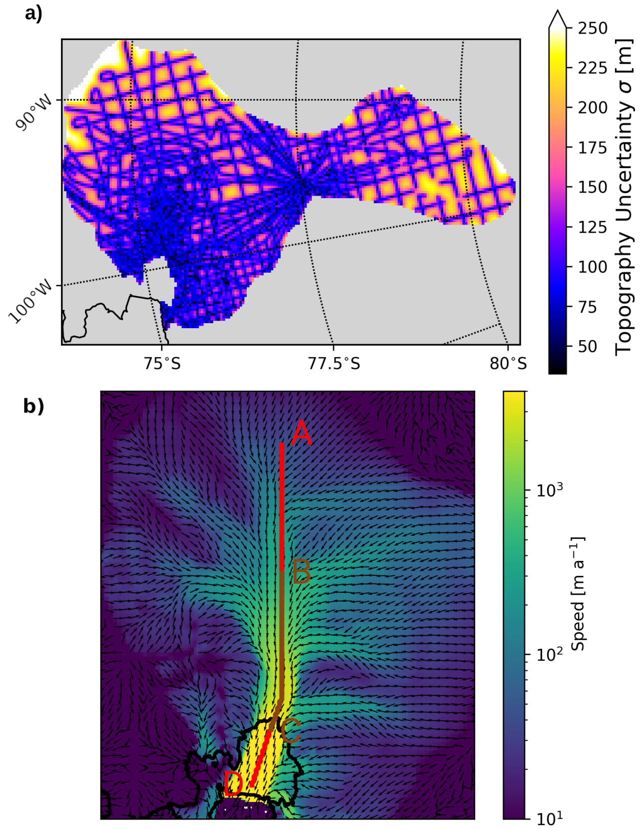

Figure 1. a: One standard deviation of trained GP which increases with distance from measurements (flight lines) and b: Initial PIG ice velocity direction (arrows) and speed (colours), for the main trunk (left half of panel a) of PIG flow including the approximate central flow line (red and brown).

ment (flight line) and is often above 50 m (one standard deviation), even in regions with close sampling.

The computational demand of sampling from a GP scales with the number of evaluated grid cells n by $\mathcal{O}(n^3)$, which imposes a limit on this number. We use the Python GPy module to draw 12 samples on a 4 km×4 km grid in the PIG catchment area. The statistically generated bedrock topographies within the grounded PIG catchment area are solely based on RES measurements and statistical modelling. However, we use Bedmap2 topography and ice thickness outside of the grounded catchment area, brought to the same resolution by averaging. This includes all locations of the Bedmap2 ice shelf mask.

The ice surface elevation is considered well known and the ice thickness is adjusted for all statistically generated topographies to match the Bedmap2 surface elevation. The resulting 12 topographies are accompanied by the Bedmap2 (Fretwell et al., 2013) and BedMachine (Morlighem, 2019; Morlighem et al., 2020) reference topographies with the same resolution.

3 Simulations

We use all combinations of the 14 topographies described above with three friction laws and two climate forcings, resulting in a total of 84 simulations. The simulations are performed by the ice sheet model BISICLES (Cornford et al., 2013, 2015), which is a finite-volume model with vertically integrated stress approximations. BISICLES combines the L1L2 approximation (Schoof & Hindmarsh, 2010) with an adaptive mesh refinement which allows for fine spatial resolutions near the GL and in fast flowing ice streams, and lower resolutions where the flow is slower and more homogeneous. The finest resolution used here is 500 m. The BISICLES inverse model framework (Cornford et al., 2015, Appendix B1) is used with a compilation of satellite based ice surface velocities from Rignot et al. (2017, 2011) to find basal traction coefficient and effective viscosity fields for each individual topography (Text S3 in the Supplement). The basal traction coefficient, effective viscosity and topography fields do not evolve over time. Figure 1b illustrates the initial velocity field of the main PIG trunk.

The Weertman friction law is :

$$\tau_b = C_m \cdot |u_b|^{m-1} \cdot u_b$$

with τ_b being the basal stress tangential to the base of the ice, C_m is the spatially varying basal traction coefficient for a given friction law exponent m and u_b is the basal ice velocity. We use $m = 1$ for linear friction, $m = 1/3$ for nonlinear friction and $m = 1/8$ for strongly nonlinear friction (called plastic friction in the following, see also Joughin et al. (2019)). Ice flow outside of the PIG catchment area is suppressed for numerical stability.

3.1 Climate forcing

We use two different climate forcings with changing ocean melt and SMB. These two forcings are intended to encompass the range of likely climate scenarios:

1. The **low forcing** uses an RCP2.6 SMB and constant-in-time ocean melt rates.
2. The **high forcing** uses an RCP8.5 SMB and linearly increasing ocean melt, starting at the low forcing rates and adding 200 % by the end of the 100-year model simulations

As SMB we use yearly output directly from NorESM1-M, a CMIP5 atmosphere-ocean coupled global climate model (Bentsen et al., 2013). Of the three models selected in Barthel et al. (2020) for the ice sheet model intercomparison project ISMIP6 (Seroussi et al., 2020), NorESM1-M has the highest rank in the CMIP5 cross-model performance analysis by Agosta et al. (2015). The simulations show below median atmospheric warming and relatively strong 21st century ocean warming compared with the multi-model ensemble (Barthel et al., 2020). The ocean melt at the beginning of the simulations is based on temperature and salinity profiles corresponding to the Warm$_0$ setup in Favier et al. (2019) which is based on oceanographic measurements from Dutrieux et al. (2014). We use an ocean melt parameterisation with a quadratic dependence on the local ocean temperature above freezing, as defined in Favier et al. (2019) as M_{quad}. The squared dependency represents a positive feedback between subshelf melting and the circulation in the cavity and this parameterisation reproduces results from coupled ocean-ice sheet model simulations relatively well (Favier et al., 2019).

Predictions of future ocean melt forcing are highly uncertain, but cannot be ignored for century-scale model simulations. The two forcings used here are designed to represent reasonable low and high melt scenarios without being bound to specific climate projections. Naughten et al. (2018) analyse and select CMIP5 model output as forcing for the regional ocean model FESOM. The ocean model predicts a year 2100 ASE ocean melt increase of about 200% (multi-model mean) to 300% (ACCESS-1.0) for RCP8.5. However, the warming should be seen largely as reversal of a known model bias which makes it very likely that the increase in melt is overestimated (Naughten et al., 2018). This overestimation might be up to about 150% in melt increase (Wernecke, 2020, Section 5.2.3). We select an increase of 200% in 100 years as a best guess upper-end melt representation. It cannot be ruled out that current ocean conditions are a positive anomaly caused by internal variability. Climate projections of ice shelf ocean melt rates for the ASE often show positive trends (Naughten et al., 2018; Alevropoulos-Borrill et al., 2020; Jourdain et al., 2020), but some projections show temporarily negative ocean temperature anomalies compared to the early 2000s (Jourdain et al., 2020; Alevropoulos-Borrill et al., 2020). We apply a constant ocean melt forcing, consistent with recent past rates, as reasonable lower-end forcing.

4 Results

4.1 Simulations

In the first years we see high-amplitude small spatial-scale rates of ice thickness change which diminish over time. This is an adjustment of the model to a self-consistent state. In retrospect we should have implemented a spin-up period in the simulations with a constant forcing before the forced projections start. Instead our simulations start with forcing, including SMB corresponding to year 2000 AD. After 15 years of simulation, corresponding to 2015 AD, the initial model adjustment becomes negligible (Text S4 and figures S3 and S4 in the Supplement), hence we choose to make all following calculations relative to the state in 2015. In this way the impact of initial adjustments on the results is minimized.

The ice geometry and flow speed along the downstream sector of the central PIG flow line (B to D in Figure 1b) is illustrated for plastic friction in Figure 2. The statistically generated topographies (right) show more variability than Bedmap2 and BedMachine (left). For low forcing the glacier thins slightly without much change of the GL position. At the same time the ice speed reduces, in particular in the fast-flowing ice shelf. A partial slowdown of the PIG is also predicted for the flow line model simulations in Gladstone et al. (2012) and is found in the optimized (central) simulations from Nias et al. (2016) for all combinations of bedrock and friction law (not shown).

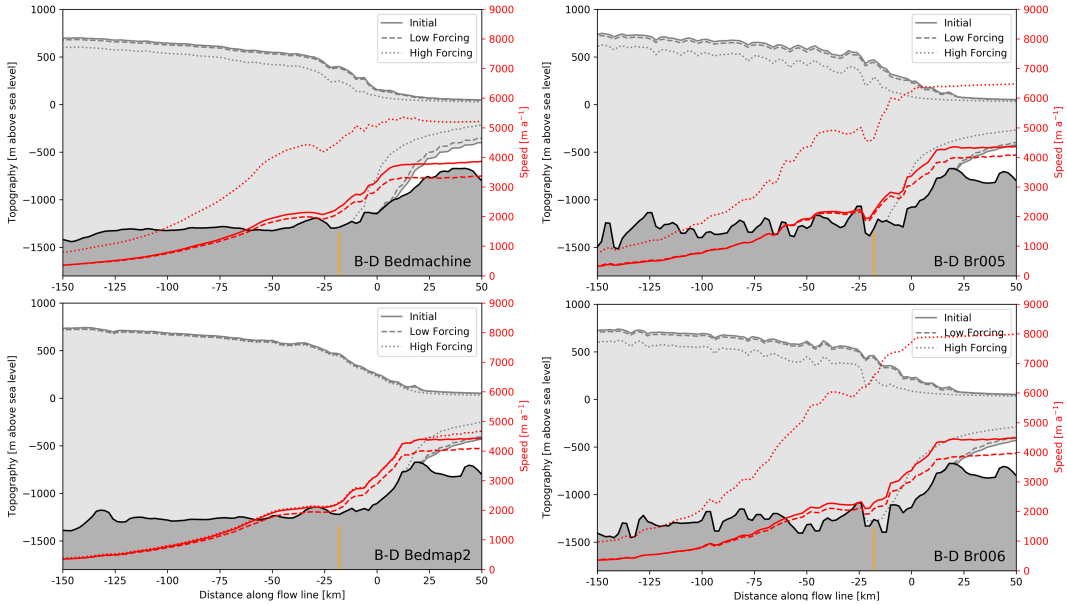

Figure 2. Profiles along PIG flow line from location B to D in Figure 1, relative to the BedMachine GL with BedMachine (top left) and Bedmap2 (bottom left) and two statistically generated topographies (right). Shown are the bedrock underneath the ice (black), surface and basal ice boundaries (grey) and the ice speed (red) after 15 years of simulation (used as baseline; solid lines) and at the end of the 100-year simulations with high (dotted) and low (dashed) forcing, all using the plastic friction law. The orange line highlights a location where Bedmap2 lies above all statistically generated topographies and BedMachine.

For the high forcing scenario we see very different pictures for BedMachine and Bedmap2 geometries: For BedMachine the ice near its GL accelerates over the 85 year projection period from less than 4000 m a^{-1} to more than 5000 m a^{-1}. The speed-up extends more than 150 km upstream (red lines in Figure 2). For Bedmap2 the high forcing scenario does not show noteworthy acceleration or thinning.

The flow line characteristics of two topographies generated here are shown on the right of Figure 2. Simulations with statistically generated topographies share the same features of those using BedMachine: little changes to the ice geometry with some slowdown of the ice for low forcing, and pronounced thinning with significant retreat of their GLs and accelerating ice for high forcing.

4.2 Sea level rise contribution

The ensemble behaviour can be categorized into two states, a steadily evolving state with approximately constant rates of mass loss (about 0.1 mm SLE a^{-1}) and an unstable state with mass losses up to six times higher (Figure 3, top). The timing of an ensemble member to become unstable depends strongly on the topography and forcing: most high melt simulation become unstable between 2055 and 2075. This timing seems not to depend on the friction law (Figure 3, top right). Low melt ensemble members remain in the steadily evolving state without exception.

The main effect of the friction law is an increase in the rate of mass loss in the unstable state with higher rates for more non-linear friction laws (Figure 3, middle). For low forcing the relationship is reversed, more linear friction leads to larger sea level

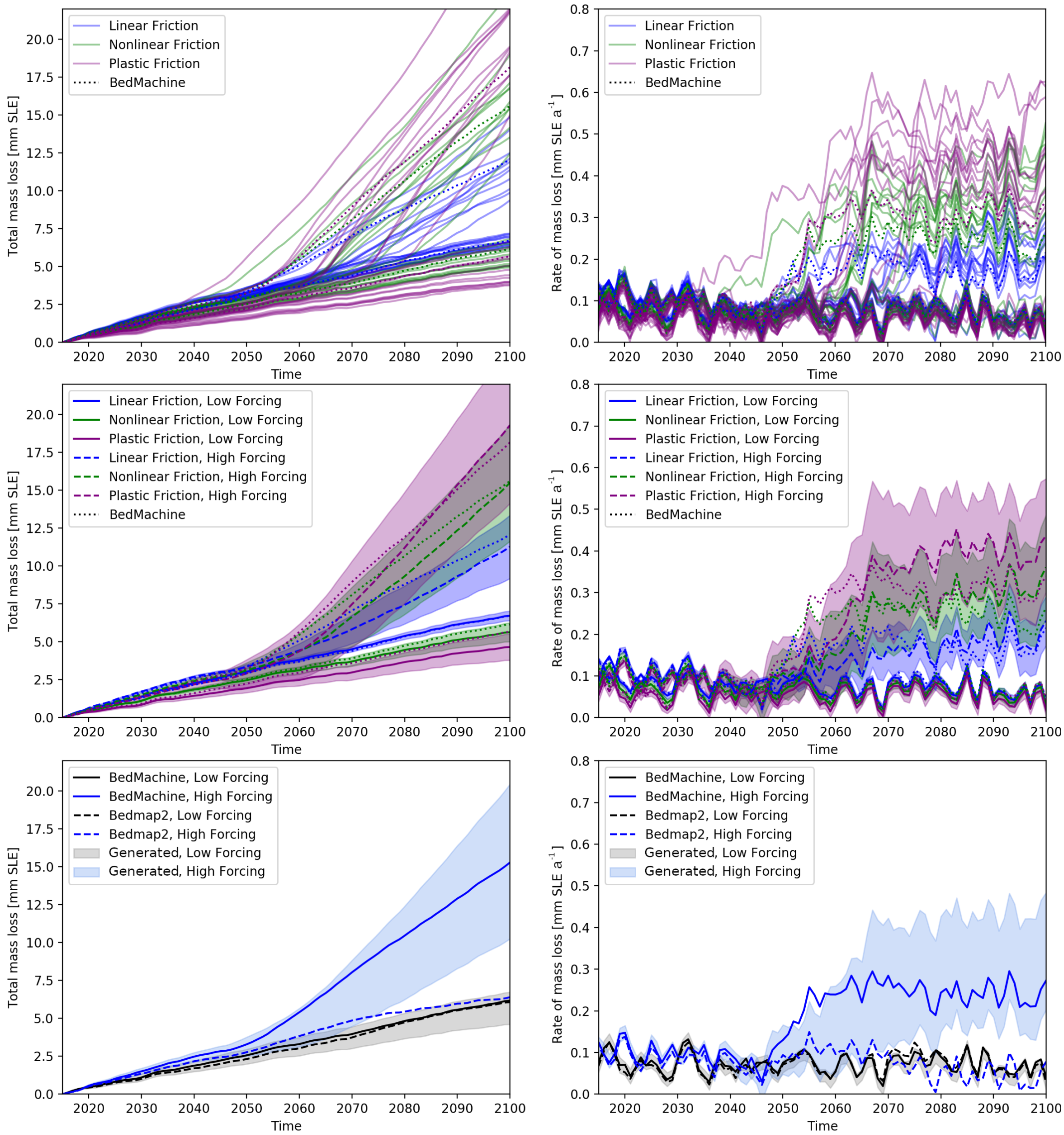

Figure 3. Net sea level contribution (left) and yearly rate (right). Individual simulations (top), grouped by friction law and forcing (middle) and grouped only by forcing including Bedmap2 (bottom). Shades correspond to ± one standard deviation.

Table 1. Mean 2100 sea level contribution estimates (relative to 2015) with one standard deviation of the statistically generated bedrock ensemble (both in mm SLE)

Friction law:	Linear	Nonlinear	Plastic
High Forcing:	11.3 ±2.08	15.5 ±3.86	19.4 ±5.15
Low Forcing:	6.7 ±0.31	5.6 ±0.62	4.7 ±0.87

contributions. This can be traced back to the slowdown of the ice as shown in Figure 2. Highly nonlinear friction laws facilitate decelerating ice to slow down even more and accelerating ice to speed up more than linear counterparts. This also explains why the predictive uncertainty due to the bedrock uncertainty strongly increases with non-linearity of the friction law and with stronger forcing. The standard deviation (STD) of the net sea level contribution over the 85 years increases with non-linearity (Table 1) which is consistent with the literature (Nias et al., 2016). The STD values range from 0.31 mm SLE for low forcing and linear friction to 5.15 mm SLE for high forcing and plastic friction which corresponds to about 5% to 25% of total sea level contribution (Figure 3 middle and Table 1).

All simulations shown here agree regarding the total sea level contribution for the low forcing scenario. However, with high forcing Bedmap2 runs are not consistent with the behaviour of simulations based on topographies generated here or BedMachine. For Bedmap2 simulations sea level rise contributions remain in the more stable, steadily evolving state regardless of forcing and friction law (Figure 3 bottom).

5 Discussion

The nonlinear response of PIG to strong forcing materializing in two distinct states is consistent with literature (Sun et al., 2014; Durand et al., 2011; Nias et al., 2018) and is in general agreement with the MISI hypothesis. None of these studies is designed to fully represent the current observational uncertainty in bedrock topography. Marine ice-cliff instability is not represented here but cannot be ruled out on these timescales. More research is needed to robustly represent marine ice-cliff instability in a well constrained way to predict how strong its impact would be on our simulations (Edwards et al., 2019).

Bedmap2 PIG simulations show less sensitivity to strong climate forcing than the statistically generated topographies and BedMachine but it is unclear what aspect of the topographies cause this response in the simulations: BedMachine uses a mass conservation approach where topographies are relaxed to avoid large mass flux divergence from inconsistent ice geometry-velocity combinations. Nias et al. (2018) supports our results in finding that a topography generated by a similar process to BedMachine exhibits a step change in mass loss which does not appear in Bedmap2 simulations. However, the topographies generated here, in common with Bedmap2, do not enforce a mass-conservation condition, share a topographic high near the Bedmap2 GL and use the same surface geometry. The fact that BedMachine does not share these characteristics, nor the same initial grounding line location, makes it even more remarkable that simulations using BedMachine and topographies generated here show consistent sea level rise contributions for both forcings. Our topographies show considerably more spatial variability in the topography than the relatively smooth Bedmap2 and BedMachine.

There are sporadic locations, including one about 20 km upstream of the BedMachine GL, where Bedmap2 topography is higher than all statistically generated topography and BedMachine (location highlighted in Figure 2, Figure S5 and Figure

S6 in the Supplement). Especially since this location is a local topographic low (Figure 2) it is not clear whether it can explain the unique behaviour of Bedmap2 (see also Text S5 in the Supplement). It is therefore unclear whether this behaviour is unique to PIG but we have been able to show that ice sheet simulations can generally be very sensitive to the bedrock topography. Whatever the exact reason, the striking underestimation of PIG mass loss for Bedmap2 simulations and high forcing relative to the other topographies (Figure 3, bottom), calls for caution in interpreting modelling projections of grounding line retreat obtained with this topography.

A limitation of our simulations is the resolution of statistically generated topographies of 4 km × 4 km (which is interpolated up to 500 m resolution within the adaptive grid refinement of BISICLES). The reason is the relatively high computational demand of a Cholesky decomposition which is used to generate random samples from a large covariance matrix. Evaluations of the mean field ('best estimate') would have been possible on fine resolutions, but would not have covered all of the uncertainties. The statistically generated topographies contain much more variability than both reference topographies and finer resolutions would, if anything, amplify this property. Nevertheless, simulations using Bedmap2 topography at 1 km resolution behave very similarly to those with degraded 4 km resolution (not shown).

To represent bedrock uncertainty in future simulations it would be desirable to have a set of topographies similar to the ones generated here but for more general setups, ideally continent-wide. This would allow different modelling groups to represent topographic uncertainty in predictions while retaining comparability. Similar approaches could be used to assess the value of additional measurements, e.g. for planning future campaigns.

In conclusion, we have been able to couple the representation of the topographic uncertainty in ice sheet simulations closely to observational constraints and demonstrate how this uncertainty interacts with other model parameters. The predictive uncertainty increases with non-linearity of the friction law and with higher melt forcing. One standard deviation can contribute between 5% and about 25% (equivalent to 5 mm SLE) of the 85-year signal, solely due to uncertainties in topography measurements and interpolation. These predictive uncertainties have been known to exist but until now remained largely omitted and unquantified. The low forcing scenario, which is more likely to be realized in very low greenhouse gas emission scenarios, would limit the PIG contribution to global mean sea level in this century. In addition we find the use of Bedmap2 to be likely to lead to an underestimation of the dynamic response of PIG to high forcing scenarios compared to the use of topographies designed explicitly to span the range of uncertainty which all suggest higher rates of mass loss.

6 Open Research

The simulations and bedrock topographies generated here are in public archive at Wernecke et al. (2021a),Wernecke et al. (2021b) and Wernecke et al. (2021c) (linear, nonlinear and plastic friction, respectively). Radio echo sounding data is available from Paden et al. (2010) and Holt, Blankenship, Corr, et al. (2006). The Python code for the statistical modelling of the representative topographies can be found at Wernecke (2021).

Acknowledgments

We would like to thank Jonty Rougier for inspirational discussions on this project. AW was supported by The Open University through a scholarship at the time of conducting this research. We acknowledge the support of the University of Bristol Advanced Computing Research Centre in providing computational resources for the

BISICLES simulations and the authors of Holt, Blankenship, Corr, et al. (2006) to provide us with an ungridded version of the data.

References

Agosta, C., Fettweis, X., & Datta, R. (2015). Evaluation of the cmip5 models in the aim of regional modelling of the antarctic surface mass balance. *The Cryosphere*, *9*, 2311–2321.

Alevropoulos-Borrill, A. V., Nias, I. J., Payne, A. J., Golledge, N. R., & Bingham, R. J. (2020). Ocean-forced evolution of the amundsen sea catchment, west antarctica, by 2100. *The Cryosphere*, *14*, 1245–1258.

Alley, R. B., Anandakrishnan, S., Christianson, K., Horgan, H. J., Muto, A., Parizek, B. R., ... Walker, R. T. (2015). Oceanic forcing of ice-sheet retreat: West antarctica and more. *Annual Review of Earth and Planetary Sciences*, *43*, 207–231.

Bamber, J. L., & Dawson, G. J. (2020). Complex evolving patterns of mass loss from antarctica's largest glacier. *Nature Geoscience*, *13*(2), 127–131.

Bamber, J. L., Westaway, R. M., Marzeion, B., & Wouters, B. (2018). The land ice contribution to sea level during the satellite era. *Environmental Research Letters*, *13*(6), 063008. doi: 10.1088/1748-9326/aac2f0

Barthel, A., Agosta, C., Little, C. M., Hattermann, T., Jourdain, N. N., Goelzer, H., ... Bracegirdle, T. T. (2020). Cmip5 model selection for ismip6 ice sheet model forcing: Greenland and antarctica. *The Cryosphere*, *14*(3), 855–879.

Bentsen, M., Bethke, I., Debernard, J. B., Iversen, T., Kirkevåg, A., Seland, Ø., ... others (2013). The norwegian earth system model, noresm1-m–part 1: description and basic evaluation of the physical climate. *Geoscientific Model Development*, *6*(3), 687–720.

Cornford, S. L., Martin, D., Payne, A., Ng, E., Le Brocq, A., Gladstone, R., ... Vaughan, D. G. (2015). Century-scale simulations of the response of the west antarctic ice sheet to a warming climate. *The Cryosphere*, *9*, 1579–1600. doi: 10.5194/tc-9-1579-2015

Cornford, S. L., Martin, D. F., Graves, D. T., Ranken, D. F., Le Brocq, A. M., Gladstone, R. M., ... Lipscomb, W. H. (2013). Adaptive mesh, finite volume modeling of marine ice sheets. *Journal of Computational Physics*, *232*(1), 529–549. doi: 10.1016/j.jcp.2012.08.037

Durand, G., Gagliardini, O., Favier, L., Zwinger, T., & Le Meur, E. (2011). Impact of bedrock description on modeling ice sheet dynamics. *Geophysical Research Letters*, *38*(20), L20501. doi: 10.1029/2011GL048892

Dutrieux, P., De Rydt, J., Jenkins, A., Holland, P. R., Ha, H. K., Lee, S. H., ... Schröder, M. (2014). Strong sensitivity of pine island ice-shelf melting to climatic variability. *Science*, *343*(6167), 174–178.

Edwards, T. L., Brandon, M. A., Durand, G., Edwards, N. R., Golledge, N. R., Holden, P. B., ... Wernecke, A. (2019). Revisiting antarctic ice loss due to marine ice-cliff instability. *Nature*, *566*(7742), 58–64. doi: 10.1038/s41586-019-0901-4

Favier, L., Durand, G., Cornford, S. L., Gudmundsson, G. H., Gagliardini, O., Gillet-Chaulet, F., ... Le Brocq, A. M. (2014). Retreat of pine island glacier controlled by marine ice-sheet instability. *Nature Climate Change*, *4*(2), 117–121. doi: 10.1038/nclimate2094

Favier, L., Jourdain, N. C., Jenkins, A., Merino, N., Durand, G., Gagliardini, O., ... Mathiot, P. (2019). Assessment of sub-shelf melting parameterisations using the ocean–ice-sheet coupled model nemo (v3. 6)–elmer/ice (v8. 3). *Geoscientific Model Development*, *12*(6), 2255–2283.

Fretwell, P., Pritchard, H. D., Vaughan, D. G., Bamber, J., Barrand, N., Bell, R., ... others (2013). Bedmap2: improved ice bed, surface and thickness datasets for antarctica. *The Cryosphere*, *7*, 375–393. doi: 10.5194/tc-7-375-2013

Gasson, E., DeConto, R., & Pollard, D. (2015). Antarctic bedrock topography uncertainty and ice sheet stability. *Geophysical Research Letters*, *42*(13), 5372–5377.

Gladstone, R. M., Lee, V., Rougier, J., Payne, A. J., Hellmer, H., Le Brocq, A., ... Cornford, S. L. (2012). Calibrated prediction of pine island glacier retreat during the 21st and 22nd centuries with a coupled flowline model. *Earth and Planetary Science Letters*, *333*, 191–199. doi: 10.1016/j.epsl.2012.04.022

Holt, J. W., Blankenship, D. D., Corr, H. F., Morse, D. L., Vaughan, D. G., & Young, D. A. (2006). Subglacial topography: Airborne geophysical survey of the amundsen sea embayment, antarctica. from nov. 2004 to mar. 2005. U.S. Antarctic Program (USAP) Data Center. doi: 10.7265/N59W0CDC

Holt, J. W., Blankenship, D. D., Morse, D. L., Young, D. A., Peters, M. E., Kempf, S. D., ... Corr, H. F. (2006). New boundary conditions for the west antarctic ice sheet: Subglacial topography of the thwaites and smith glacier catchments. *Geophysical Research Letters*, *33*(9), L09502. doi: 10.1029/2005GL025561

Joughin, I., & Alley, R. B. (2011). Stability of the west antarctic ice sheet in a warming world. *Nature Geoscience*, *4*(8), 506–513.

Joughin, I., Smith, B. E., & Medley, B. (2014). Marine ice sheet collapse potentially under way for the thwaites glacier basin, west antarctica. *Science*, *344*(6185), 735–738. doi: 10.1126/science.1249055

Joughin, I., Smith, B. E., & Schoof, C. G. (2019). Regularized coulomb friction laws for ice sheet sliding: Application to pine island glacier, antarctica. *Geophysical Research Letters*, *46*(9), 4764–4771. doi: 10.1029/2019GL082526

Jourdain, N. C., Asay-Davis, X., Hattermann, T., Straneo, F., Seroussi, H., Little, C. M., & Nowicki, S. (2020). A protocol for calculating basal melt rates in the ismip6 antarctic ice sheet projections. *The Cryosphere*, *14*(9), 3111–3134.

Milillo, P., Rignot, E., Mouginot, J., Scheuchl, B., Morlighem, M., Li, X., & Salzer, J. T. (2017). On the short-term grounding zone dynamics of pine island glacier, west antarctica, observed with cosmo-skymed interferometric data. *Geophysical Research Letters*, *44*(20), 10–436.

Morlighem, M. (2019). Measures bedmachine antarctica, version 1. Boulder, Colorado USA. NASA National Snow and Ice Data Center Distributed Active Archive Center. (Accessed: 2020-02) doi: 10.5067/C2GFER6PTOS4

Morlighem, M., Rignot, E., Binder, T., Blankenship, D., Drews, R., Eagles, G., ... others (2020). Deep glacial troughs and stabilizing ridges unveiled beneath the margins of the antarctic ice sheet. *Nature Geoscience*, *13*(2), 132–137. doi: 10.1038/s41561-019-0510-8

Mouginot, J., Rignot, E., & Scheuchl, B. (2014). Sustained increase in ice discharge from the amundsen sea embayment, west antarctica, from 1973 to 2013. *Geophysical Research Letters*, *41*(5), 1576–1584.

Mouginot, J., Scheuchl, B., & Rignot, E. (2017). Measures antarctic boundaries for ipy 2007-2009 from satellite radar, version 2. Boulder, Colorado USA. NASA National Snow and Ice Data Center Distributed Active Archive Center. (Accessed: 2019-07) doi: 10.5067/AXE4121732AD

Naughten, K. A., Meissner, K. J., Galton-Fenzi, B. K., England, M. H., Timmermann, R., & Hellmer, H. H. (2018). Future projections of antarctic ice shelf melting based on cmip5 scenarios. *Journal of Climate*, *31*(13), 5243–5261.

Nias, I. J., Cornford, S., & Payne, A. (2018). New mass-conserving bedrock topography for pine island glacier impacts simulated decadal rates of mass loss. *Geophysical Research Letters*, *45*(7), 3173–3181. doi: 10.1002/2017GL076493

Nias, I. J., Cornford, S. L., & Payne, A. J. (2016). Contrasting the modelled sensitivity of the amundsen sea embayment ice streams. *Journal of Glaciology*, *62*(233), 552–562. doi: 10.1017/jog.2016.40

Oppenheimer, M., Glavovic, B., Hinkel, J., van de Wal, R., Magnan, A. K., Abd-

Elgawad, A., … Sebesvari, Z. (2019). Sea level rise and implications for low lying islands, coasts and communities. In *Ipcc special report on the ocean and cryosphere in a changing climate [h.-o. portner, d.c. roberts, v. masson-delmotte, p. zhai, m. tignor, e. poloczanska, k. mintenbeck, a. alegria, m. nicolai, a. okem, j. petzold, b. rama, n.m. weyer (eds.)].* The Intergovernmental Panel on Climate Change.

Paden, J., Li, J., Leuschen, C., Rodriguez-Morales, F., & Hale, R. (2010). Icebridge mcords l2 ice thickness, version 1. from oct. 2009 to dec. 2017. Boulder, Colorado USA. NASA National Snow and Ice Data Center Distributed Active Archive Center. (updated 2019, Accessed: 2019-09) doi: 10.5067/GDQ0CUCVTE2Q

Rasmussen, C. E., & Williams, C. K. (2006). *Gaussian processes for machine learning* (Vol. 2) (No. 3). MIT Press Cambridge, MA.

Rignot, E., Bamber, J. L., Van Den Broeke, M. R., Davis, C., Li, Y., Van De Berg, W. J., & Van Meijgaard, E. (2008). Recent antarctic ice mass loss from radar interferometry and regional climate modelling. *Nature Geoscience*, *1*(2), 106–110. doi: 10.1038/ngeo102

Rignot, E., Jacobs, S., Mouginot, J., & Scheuchl, B. (2013). Ice-shelf melting around antarctica. *Science*, *341*(6143), 266–270.

Rignot, E., Mouginot, J., Morlighem, M., Seroussi, H., & Scheuchl, B. (2014). Widespread, rapid grounding line retreat of pine island, thwaites, smith, and kohler glaciers, west antarctica, from 1992 to 2011. *Geophysical Research Letters*, *41*(10), 3502–3509. doi: 10.1002/2014GL060140

Rignot, E., Mouginot, J., & Scheuchl, B. (2017). Measures insar-based antarctica ice velocity map, version 2. Boulder, Colorado USA. NASA National Snow and Ice Data Center Distributed Active Archive Center. (Accessed: 2018-11) doi: 10.5067/D7GK8F5J8M8R

Rignot, E., Velicogna, I., van den Broeke, M. R., Monaghan, A., & Lenaerts, J. T. (2011). Acceleration of the contribution of the greenland and antarctic ice sheets to sea level rise. *Geophysical Research Letters*, *38*(5), L05503. doi: 10.1029/2011GL046583

Schlegel, N.-J., Seroussi, H., Schodlok, M. P., Larour, E. Y., Boening, C., Limonadi, D., … Broeke, M. R. (2018). Exploration of antarctic ice sheet 100-year contribution to sea level rise and associated model uncertainties using the issm framework. *The Cryosphere*, *12*(11), 3511–3534. doi: 10.5194/tc-12-3511-2018

Schoof, C. (2007). Ice sheet grounding line dynamics: Steady states, stability, and hysteresis. *Journal of Geophysical Research: Earth Surface*, *112*(F3), F03S28.

Schoof, C., & Hindmarsh, R. C. (2010). Thin-film flows with wall slip: an asymptotic analysis of higher order glacier flow models. *Quarterly Journal of Mechanics and Applied Mathematics*, *63*(1), 73–114. doi: 10.1093/qjmam/hbp025

Seroussi, H., Nowicki, S., Payne, A. J., Goelzer, H., Lipscomb, W. H., Abe Ouchi, A., … Zwinger, T. (2020). Ismip6 antarctica: a multi-model ensemble of the antarctic ice sheet evolution over the 21st century. *The Cryosphere*. doi: 10.5194/tc-14-3033-2020

Shepherd, A., Ivins, E., Rignot, E., Smith, B., Van Den Broeke, M., Velicogna, I., … Wouters, B. (2018). Mass balance of the antarctic ice sheet from 1992 to 2017. *Nature*, *558*, 219–222. doi: 10.1038/s41586-018-0179-y

Sun, S., Cornford, S., Liu, Y., & Moore, J. C. (2014). Dynamic response of antarctic ice shelves to bedrock uncertainty. *The Cryosphere*, *8*(4), 1561–1576.

Wernecke, A. (2020). *Quantifying century-scale uncertainties of the global mean sea level rise contribution from the amundsen sea sector, west antarctica* (Doctoral dissertation, The Open University). doi: 10.21954/ou.ro.0001223d

Wernecke, A. (2021, December). *script to generate stat. samples of PIG topography* *with Gaussian Process model.* Zenodo. Retrieved from `https://doi.org/10.5281/zenodo.5788669` doi: 10.5281/zenodo.5788669

Wernecke, A., Tamsin, L., Edwards, Holden, B., Philip, Edwards, N. R., & Cornford, S. L. (2021a, October). *BISICLES Pine Island Glacier simulations with linear friction.* Zenodo. Retrieved from `https://doi.org/10.5281/zenodo.5553288` doi: 10.5281/zenodo.5553288

Wernecke, A., Tamsin, L., Edwards, Holden, B., Philip, Edwards, N. R., & Cornford, S. L. (2021b, October). *BISICLES Pine Island Glacier simulations with nonlinear friction.* Zenodo. Retrieved from `https://doi.org/10.5281/zenodo.5553311` doi: 10.5281/zenodo.5553311

Wernecke, A., Tamsin, L., Edwards, Holden, B., Philip, Edwards, N. R., & Cornford, S. L. (2021c, October). *BISICLES Pine Island Glacier simulations with strongly nonlinear friction.* Zenodo. Retrieved from `https://doi.org/10.5281/zenodo.5553320` doi: 10.5281/zenodo.5553320

Zhao, C., Gladstone, R. M., Warner, R. C., King, M. A., Zwinger, T., & Morlighem, M. (2018). Basal friction of fleming glacier, antarctica–part 1: Sensitivity of inversion to temperature and bedrock uncertainty. *The Cryosphere*, *12*(8), 2637–2652.

1

Supporting Information for "Quantifying the impact of bedrock topography uncertainty in Pine Island Glacier projections for this century"

Andreas Wernecke[1,2,3], Tamsin L. Edwards[4], Philip B. Holden[1], Neil R. Edwards[1], Stephen L. Cornford [5]

[1]The Open University, Milton Keynes, UK

[2]Max-Planck-Institute for Meteorology, Hamburg, Germany

[3]Universitt Hamburg, Hamburg, Germany

[4]Kings Collage London, London, UK

[5]Faculty of Science and Engineering, Swansea University, Swansea, UK

Contents of this file

1. Text S1 to S5
2. Figures S1 to S6
3. Table S1

Additional Supporting Information (Files uploaded separately)

1. Movie S1 to S4

Text S1.

1. RES data inconsistencies

By careful inspection we asses the consistency of the radio echo sounding data. In particular we inspect the ice thickness estimates and search for (1) sudden and sustained changes along flight lines (e.g. as highlighted at the bottom of Figure S1) and (2) sections of flight line ice thickness estimates which cross several other flight lines and have sustained different values (e.g. as highlighted in the center of Figure S1). These two criteria are often found in conjunction. Note that Figure S1 is not the final dataset used here, but illustrates the process of identifying inconsistencies.

Text S2.

2. Statistical properties of the bedrock topography

The information in this section is taken from Wernecke (2020), with minor adjustments, and repeated here for the readers' convenience.

2.1. Gaussian Process modelling

In the following we will describe our approach to generating new bedrock topographies in more detail. The main novelty is that we use a stochastic model to represent the bedrock topography at each location as a random variable and represent uncertainties in these random variables (the spread) by sampling spatial fields of bedrock topography which inhabit the local uncertainties and spatial covariance structure.

The bedrock can be understood as continuous random variable B, approximated as a Gaussian Process,

$$B = G(\vec{\bar{b}}(\vec{z}, \vec{\theta}),\ c(\vec{\theta})), \tag{1}$$

where $G(\cdot, \cdot)$ denotes a Gaussian Process. The bedrock topography at each location in the horizontal model domain is therefore considered a random variable with Gaussian distribution centered at $\vec{\bar{b}}(\vec{z}, \vec{\theta})$, depending on the observations $\vec{z}$ with covariance between locations defined by the covariance function $c(\vec{\theta})$. The covariance function parameters $\vec{\theta}$ define among other things the length scale of decorrelation, or in other words, how informative the topography at one location is for the topography at surrounding locations. We do not use a reference topography as prior nor do we subtract any mean function in order to ensure independence from all published datasets. This will allow us to investigate the consistency between the topographies statistically generated here and reference topographies (Bedmap2 and Bedmachine) in the following analysis.

We assume the existence of an optimal set of covariance function parameters $\vec{\theta^*}$ and constrain estimates of $\vec{\theta^*}$ with observations. To asses these covariance function parameters we will in this section describe the analysis in more detail than possible in the main text. Using conditional likelihoods we can express Equation 1 as:

$$B = G(\vec{\bar{b}}(\vec{z}, \vec{\theta^*}),\ c(\vec{\theta^*}))\,|\vec{\theta^*} \cdot \pi(\vec{\theta^*}|\vec{z}) \cdot \pi(\vec{z}) \tag{2}$$

Due to computational constraints we have to use subsets of the whole set of observations ($\vec{z}$), with $\vec{z_1}$ of $\mathcal{O}(10\,000)$ measurements for $\vec{\bar{b}}(\vec{z}, \vec{\theta^*})$ and $\vec{z_2}$ of $\mathcal{O}(100\,000)$ for $\pi(\vec{\theta^*}|\vec{z})$. The reason for the different sample sizes is that the computational expense associated with the size of $\vec{z_1}$ is of $\mathcal{O}(n^3)$ the expense associated with the size of $\vec{z_2}$ is of $\mathcal{O}(n^2)$ (see below). Equation 2 becomes:

$$B = G(\vec{\bar{b}}(\vec{z_1}, \vec{\theta^*}),\ c(\vec{\theta^*}))\,|\vec{\theta^*} \cdot \pi(\vec{\theta^*}|\vec{z_2}) \cdot \pi(\vec{z_2}) \tag{3}$$

We constrain $\pi(\vec{\theta^*}|\vec{z_2})$ using semivariograms. In semivariograms the distances between all possible pairs of $\vec{z_2}$ are binned, in our case in 250 m intervals and the covariance between all pairs within each interval is calculated. It therefore illustrates how the correlation in topography elevation diminishes with distance and can be used to infer the nugget (variance at a distance of zero), range (characteristic correlation length scale) and sill (far field variance) by a least squared error fit. We use an exponential function for the semivariogram fit and the covariance function of the GP model which allows us to use the fitted parameters as our best estimate of θ^*. A limitation of using semivariograms to find the covariance function is the possible dependency of $\pi(\vec{\theta^*}|\vec{z_2})$ on the size of the domain examined for the semivariograms. This additional uncertainty is taken into account by using six different domains, from [0 km, 25 km] to [0 km, 50 km] (see Figure S2). That is from the approximate width of contributory glaciers of PIG (25 km) to approximately the largest data gap between flight-lines in the catchment area (50 km). The spatial characteristics on scales larger than this will be well constrained by the observations themselves. Note that the range parameter can lie outside of this domain, as this is merely the domain used for fitting. The total number of pairs n samples can build is $n(n-1)/2$, which explains why the computational cost of semivariograms scales with $\mathcal{O}(n^2)$.

The distribution of $\pi(\vec{z_2})$ is represented by repeated random sub-sampling of $\vec{z_2}$ from $\vec{z}$. Six different sets of $\vec{z_2}$ are then used for $\pi(\vec{\theta^*}|\vec{z_2})$ together with six different fitting domains, increasing the upper bound in 5 km steps from 25 to 50 km to represent the distribution of $\pi(\vec{\theta^*}|\vec{z_2})$. The six resulting semivariograms are shown in Figure S2 and the corresponding estimates of θ^* are shown in Table S1. The relatively small spread of estimates of θ^* (Table S1) illustrates that the combined impact of sub-sampling and fitting interval size on θ^* is small, supporting the robustness of this approach. All those estimates are used successively for the GP model $G(\vec{b}(\vec{z_1}, \vec{\theta^*}),\ c(\vec{\theta^*}))\,|\vec{\theta^*}$ (technically these are six separate GP models which are handled in the same way at all times). In order to ensure good spatial coverage by $\vec{z_1}$ we impose a regular grid with 2 km resolution on the region and randomly select one measurement from each non-empty grid cell. This semi-random selection is repeated for each estimate of θ^*.

To address the correspondence of parameters from the semivariogram fit and the covariance function it can be illustrative to discuss particularly the role of σ_c^2. It is derived as the sill of the exponential fit to the semivariance, representing the semivariance at large distances where spatial correlations are negligible and enters the covariance function as scaling parameter of the exponentially decaying covariance. For very small distances r, $COV(x_i, x_i) \approx \sigma_c^2$. The covariance of the topography at x_i with x_i is simply the variance at this location. The semivariance (y) for a given distance (r) between the locations x_i and x_j is defined as: $y(x_i, x_j) = 0.5 \cdot VAR(f(x_i) - f(x_j))$, where $f()$ represents the mapping of locations to topography values. For locations far from each other ($r \gg \ell$) the topography is considered uncorrelated so that the semivariance simplifies to:

$$y(x_i, x_j) = 0.5 \cdot VAR(f(x_i)) + 0.5 \cdot VAR(f(x_j)).$$

We have seen before that for our covariance function, the variance at x_i approaches σ_c^2, so that $y(x_i, x_j) = \sigma_c^2$ if x_i and x_j are far from each other. Therefore the parameter σ_c in the covariance function can be approximated by the sill of the semivariance. In other words, the semivariance is reduced where the covariance is still large, but the maximum semivariance (σ_c^2) informs the total variance which is defined by the covariance at very small r.

Considering a set of training point locations $\vec{x_1}$ with corresponding topography values $\vec{z_1}$, the random distribution of a GP model at a new, finite set of locations $\vec{x_*}$ is found (see e.g. Rasmussen and Williams (2006)) by:

$$G(\vec{\bar{b}}(\vec{z_1}, \vec{\theta^*}),\ c(\vec{\theta^*})) = N(\vec{\bar{b}}(\vec{z_1}, \vec{\theta^*}), \mathbf{\Sigma}_*) \tag{4}$$

$$\vec{\bar{b}}(\vec{z_1}, \vec{\theta^*}) = K(\vec{x_*}, \vec{x_1}) K(\vec{x_1}, \vec{x_1})^{-1} \vec{z_1} \tag{5}$$

$$\mathbf{\Sigma}_* = K(\vec{x_*}, \vec{x_*}) - K(\vec{x_*}, \vec{x_1}) K(\vec{x_1}, \vec{x_1})^{-1} K(\vec{x_1}, \vec{x_*})) \tag{6}$$

where $N(\vec{\mu}, \mathbf{\Sigma})$ represents a multivariate normal distribution with mean vector $\vec{\mu}$ and covariance matrix $\mathbf{\Sigma}$. The values of $K(\vec{x}, \vec{x})_{ij} = c(\vec{x_i}, \vec{x_j})$ are derived from evaluations of the GP covariance function $c(\cdot, \cdot)$ of the ith and jth member of $\vec{x}$ (see covariance equation in the main text). The diagonal of $\mathbf{\Sigma}_*$ is the total variance at locations $\vec{x_*}$, as shown, in terms of its square root, in Figure 1(a) and shading in Figure S5.

2.2. GP samples

For the application in this work it is essential that the samples from the Gaussian Process (GP) are continuous so that no unreasonable jumps in the topography are created. The only way to ensure continuous samples, representing the full PIG topography covariance structure is to avoid any subdivision of the PIG basin in the topography generation process. As will be shown in the following, this influences the numerical demands and achievable topography resolution of this approach.

We use the GPy Python toolbox (specifically: posterior_samples_f()) to generate those samples. It is however informative to follow Rasmussen and Williams (2006, Section A.2) to give a short introduction on how samples can be generated without a specific toolbox. A scalar random number generator and an implementation of a Cholesky decomposition algorithm will be assumed, both widely available in mathematical software. First we use the Cholesky decomposition to find the lower triangular matrix L for the positive-definite symmetric covariance matrix $\mathbf{\Sigma}_G$ which satisfies $LL^T = \mathbf{\Sigma}_G$. $\mathbf{\Sigma}_G$ is the GP covariance matrix with element i,j: $\mathbf{\Sigma}_{G,i,j} = COV(x_i, x_j)$. We then generate n_* independent standard-normally distributed random numbers stacked to the vector $\vec{p}$ where n_* is the number of evaluation points $\vec{x_*}$. A sample of the distribution G is then found by $\vec{o_*} = \vec{\mu}_G + L\vec{p}$, where $\vec{\mu}_G$ is the mean field of the GP. By construction the covariance matrix of $\vec{o_*}$ is $\mathbf{E}[\vec{o_*}\vec{o_*}^T] = L\mathbf{E}[\vec{p}\vec{p}^T]L^T = LL^T = \mathbf{\Sigma}_G$. Cholesky decompositions scale with order n^3, creating comparable restrictions for the number of training data for GPs without additional approximations and evaluation locations of GP samples. On modern workstations this limit is of the order of a few 10 000 evaluation locations.

Text S3.

3. Model Inversion

The information in this section is taken from Wernecke (2020), with minor adjustments, and repeated here for the readers' convenience.

Each topography is used separately to find basal traction coefficient and effective viscosity fields for PIG using the BISICLES inverse model framework with surface velocities from (Rignot et al., 2017, 2011) which have been re-gridded from 450 m to 1 km resolution using bilinear interpolation. The velocity data have been compiled from a large range of satellite missions, spanning in total the period from 1996 to 2016. It should however be noted that the data acquisition is not homogeneous throughout time. For example, only two of eight satellite missions used provide any data before 2006 and the start of the Landsat-8 and Sentinel-1 missions in 2013/2014 creates elevated data density towards the end of the 20-year period.

All datasets used for model inversion and initialisation are collected relatively close to the the year 2000 and even though a robust definition of a start year is challenging, the timestamp of the SMB forcing allows us to date the start of the simulations to year 2000 AD.

We use a linear Weertman friction law for inversions as in our experience it increases numerical stability in the optimisations compared with nonlinear Weertman friction laws. The effective viscosity is not influenced by the friction law but the inverted fields of basal traction coefficients have to be transformed to nonlinear equivalents as described below. The Weertman friction law is:

$$\tau_b = C_m \cdot |u_b|^{m-1} \cdot u_b$$

with $m = 1$ for linear friction, $m = 1/3$ for nonlinear friction and $m = 1/8$ for strongly nonlinear friction. In the following we will refer to the $m = 1/8$ friction law as plastic friction law (see also Joughin, Smith, and Schoof (2019)). Here τ_b is the basal stress tangential to the base of the ice, C_m is the spatially varying basal traction coefficient for a given friction law exponent m and u_b is the basal ice velocity. With the optimal initial basal shear stress τ_b being independent of the friction law it follows that

$$C_1 \cdot |u_{b0}|^0 \cdot u_{b0} = C_{1/3} \cdot |u_{b0}|^{(-2/3)} \cdot u_{b0}$$

and hence $C_{1/3} = C_1 |u_{b0}|^{(2/3)}$, where u_{b0} is the basal velocity at the beginning of the model period (as used for the inversion). An equivalent transformation is performed for plastic friction with $m = 1/8$.

Ice flow outside of the catchment area is expected to have minimal influence on the PIG flow. Therefore we drastically increase the basal traction coefficient for all friction laws to 10^6 Ns m^{-3} for grounded areas outside of the catchment area to effectively prevent ice from flowing. This is done for numerical stability at the quadratic domain boundaries and for numerical speed since suppressed ice flow allows the adaptive mesh to use lower resolutions.

Text S4.

4. Initial model behaviour

The information in this section is taken from Wernecke (2020), with minor adjustments, and repeated here for the readers' convenience.

Here we address the initial model behaviour and define a reference year for later projections. Figure S3 shows the yearly change in ice thickness (ds/dt, based on finite differences of the yearly data) for one of the randomly generated ensemble members (set B_r) with low forcing and plastic friction as an example. In the first years we see high-amplitude small-spatial-scale rates of ice thickness change which diminish with time to larger scale rates with smaller amplitude (as can be seen for year 15 of the simulation in Figure S3). These initial very high rates of ice thickness change can be attributed to an adjustment of the model to a self-consistent state. It indicates that, before adjusting, the flow regime and geometry are initially inconsistent with the model physics. The challenge here is to define the time when the persistent response dominates over the initial adjustments.

In retrospect we should have implemented a spin-up period in the simulations with a constant forcing (ocean melt and SMB) for the model to find a self-consistent state before the forced projections start. Instead the imposed SMB in all of our simulations use estimates for year 2000 in the beginning of the simulations which is why we define the beginning of the simulations as year 2000. In the same way, the basal melt starts to increase from the first year in the high forcing runs. In the following we will instead define a reference year which is used as baseline for calculations, e.g. of sea level rise contributions, in order to minimize the impact of initial adjustments on the results.

Defining a reference year by inspecting each of the 84 ensemble members (12+2 topographies times two forcings and three friction laws) in the style of Figure S3 is impractical. Therefore we calculate the spatial mean of the absolute ds/dt values and plot the development for each ensemble member using a B_r, Bedmap2 or BedMachine topography in Figure S4. Following a maximum ice thickness change in the first year, all ensemble members level out to a stable rate after a few decades or less. Bedmap2 and BedMachine start from slightly lower values in the beginning but take a similar period of time to reach a stable rate. It is not clear whether this slightly reduced period of adjustment indicates a more consistent initial state or reflects the smoother nature of those topographies. Based on Figure S4 we choose the 15th year of simulation as reference and consider this a conservative (on the larger end) value.

Text S5.

5. Possible explanations for the outlier behaviour of Bedmap2 simulations

In this section we discuss possible explanations for the outlier behaviour of Bedmap2 simulations, which remain in a steadily evolving state even for strong increasing ocean melt and RCP8.5 SMB. As stated in the main text, we cannot conclusively identify the cause of this behaviour but can show that there is no particular topographic height or feature in the basal friction field that offers a likely explanation.

5.1. Comparison of the topographic maps

Figure S5 shows all topographies used here, and the GP mean field, which was not used for the simulations. It can be seen that the GP mean and Bedmachine agree well along this flowline. Bedmap2 largely follows the same shape but is some 50 m higher. In two dimensions (Figure S6) a similar picture emerges. The average of the statistically generated fields is largely below Bedmap2 but this offset is relatively homogeneous within the main trunk of PIG (along the line in Figure S6, left). There are only sporadic locations where Bedmap2 is above (red) or below (blue) all individual members of the statistically generated ensemble (Figure S6, right). There are a few grid cells where Bedmap2 is higher than all statistically generated topographies (red cells highlighted by orange frame in Figure S6, right) which resembles what could be interpreted as topographic elevation crossing the PIG trunk. However these consist of only approximately three grid cells which are not always adjacent. In fact, this corresponds not to a topographic high but a local depression which is also highlighted by an orange line in Figure S5 about 20 km upstream of the GL. A less deep depression in Bedmap2 compared to the other topographies is not as straightforward to associate dynamically with flow stabilization than a topographic high. Nevertheless, Nias, Cornford, and Payne (2018) argue that a small regional depression (20-30 m in amplitude, 4 km in diameter) can cause an dynamic thinning impulse which propagates upstream and is sustained even when another stabilising GL location is reached.

Figure 2 in the main text shows a topographic high near the GLs of the statistically generated topographies and Bedmap2. Considering the different behaviour of simulations on those topographies, this rise is not a defining factor for the response. This seems to be because the topographic high is hardly in contact with the ice in the first place. This could (but does not have to be) a sign that the reason for Bedmap2 to have this topographic high is the misclassification of RES reflection from the bottom of a floating ice shelf as topographic reflections from grounded ice. In that case the base of the falsely assumed-grounded ice would coincide with the hydrostatic equilibrium and hence unground very easily. The statistically generated topographies have the same topographic high because they use the Bedmap2 geometry where no clear contact with the ground can be established. We use the Bedmap2 ice shelf mask to distinguish between grounded and ungrounded locations in the topography generation process, which is derived directly from satellite observations.

5.2. Basal friction coefficient

All topographies have their own inversion for basal friction coefficients which are held constant for the simulations. In the supplemented media (.gif) files we show animations of the grounding line retreating within the 100-year long simulations for Bedmap2, Bedmachine and two statistically generated topographies along with the basal friction coefficients (in all cases with strongly nonlinear friction law and strong forcing). This highlights the existence of linear features across the PIG trunk in all cases and shows how the retreat of the corresponding grounding lines is influenced by these features. The initial situation for the statistically generated topographies and Bedmap2 is such that the closest linear feature of high friction is not close to the grounding line. For the statistically generated topograpies the retreat is much faster and widespread, not through a specific gap in a high-friction feature, while for Bedmap2 there is limited retreat. The initial Bedmachine GL is much closer to a linear high friction feature compared to the other topographies used, the grounding line subsequently retreats, starting at the southern side of the ice stream and settling temporarily at a second, upstream high-friction feature later in the simulation. Again, we cannot identify a particular feature in the friction coefficient that would be a likely explanation for the difference in simulation behaviour.

We further note that the Bedmap2 topography lies largely above the others within the first approximately 150 km upstream from the GL (Figure S5) and that, for the same surface elevation of the ice, an elevated topography is further from hydrostatic equilibrium and could hence be less prone to retreat. The about 50 m difference in ice thickness corresponds to an additional couple of metres of ice which need to be removed before ungrounding, which is small compared to the locally more than 250 m of melt per year. This indicates that the, on average, higher Bedmap2 topography and its corresponding thinner ice thickness alone is not a likely explanation for the outlier behaviour of Bedmap2 simulations either.

References

Holt, J. W., Blankenship, D. D., Morse, D. L., Young, D. A., Peters, M. E., Kempf, S. D., ... Corr, H. F. (2006). New boundary conditions for the west antarctic ice sheet: Subglacial topography of the thwaites and smith glacier catchments. *Geophysical Research Letters*, *33*(9), L09502. doi: 10.1029/2005GL025561

Joughin, I., Smith, B. E., & Schoof, C. G. (2019). Regularized coulomb friction laws for ice sheet sliding: Application to pine island glacier, antarctica. *Geophysical Research Letters*, *46*(9), 4764–4771. doi: 10.1029/2019GL082526

Nias, I. J., Cornford, S., & Payne, A. (2018). New mass-conserving bedrock topography for pine island glacier impacts simulated decadal rates of mass loss. *Geophysical Research Letters*, *45*(7), 3173–3181. doi: 10.1002/2017GL076493

Paden, J., Li, J., Leuschen, C., Rodriguez-Morales, F., & Hale, R. (2010). Icebridge mcords l2 ice thickness, version 1. from oct. 2009 to dec. 2017. Boulder, Colorado USA. NASA National Snow and Ice Data Center Distributed Active Archive Center. (updated 2019, Accessed: 2019-09) doi: 10.5067/GDQ0CUCVTE2Q

Rasmussen, C. E., & Williams, C. K. (2006). *Gaussian processes for machine learning* (Vol. 2) (No. 3). MIT Press Cambridge, MA.

Rignot, E., Mouginot, J., & Scheuchl, B. (2017). Measures insar-based antarctica ice velocity map, version 2. Boulder, Colorado USA. NASA National Snow and Ice Data Center Distributed Active Archive Center. (Accessed: 2018-11) doi: 10.5067/D7GK8F5J8M8R

Rignot, E., Velicogna, I., van den Broeke, M. R., Monaghan, A., & Lenaerts, J. T. (2011). Acceleration of the contribution of the greenland and antarctic ice sheets to sea level rise. *Geophysical Research Letters*, *38*(5), L05503. doi: 10.1029/2011GL046583

Wernecke, A. (2020). *Quantifying century-scale uncertainties of the global mean sea level rise contribution from the amundsen sea sector, west antarctica* (Doctoral dissertation, The Open University). doi: 10.21954/ou.ro.0001223d

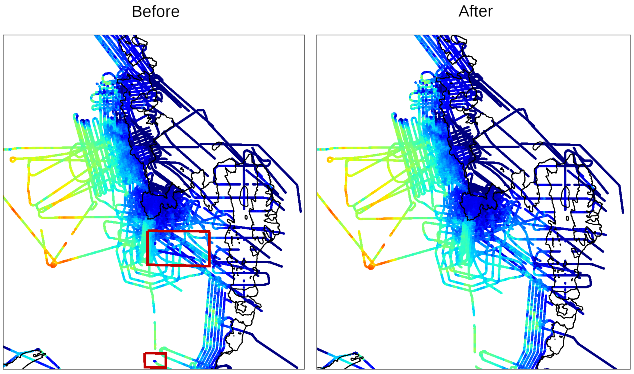

Figure S1. Ungridded RES ice thickness estimates (from zero - dark blue to 2300 m - red) before (left) and after (right) removal of some inconsistent data. Locations inconsistent data are highligterd by red rectangles. Data from Holt et al. (2006) and Paden et al. (2010)

Table S1. Estimates of $\vec{\theta^*}$

	θ^*_{25}	θ^*_{30}	θ^*_{35}	θ^*_{40}	θ^*_{45}	θ^*_{50}
Fitting interval [km]	25	30	35	40	45	50
Nugget σ_n^2 $[m^2]$	563	647	652	477	583	661
Range ℓ [km]	19	18	18	17	19	20
Sill α^2 $[\times 10^3 m^2]$	82	82	79	79	83	86

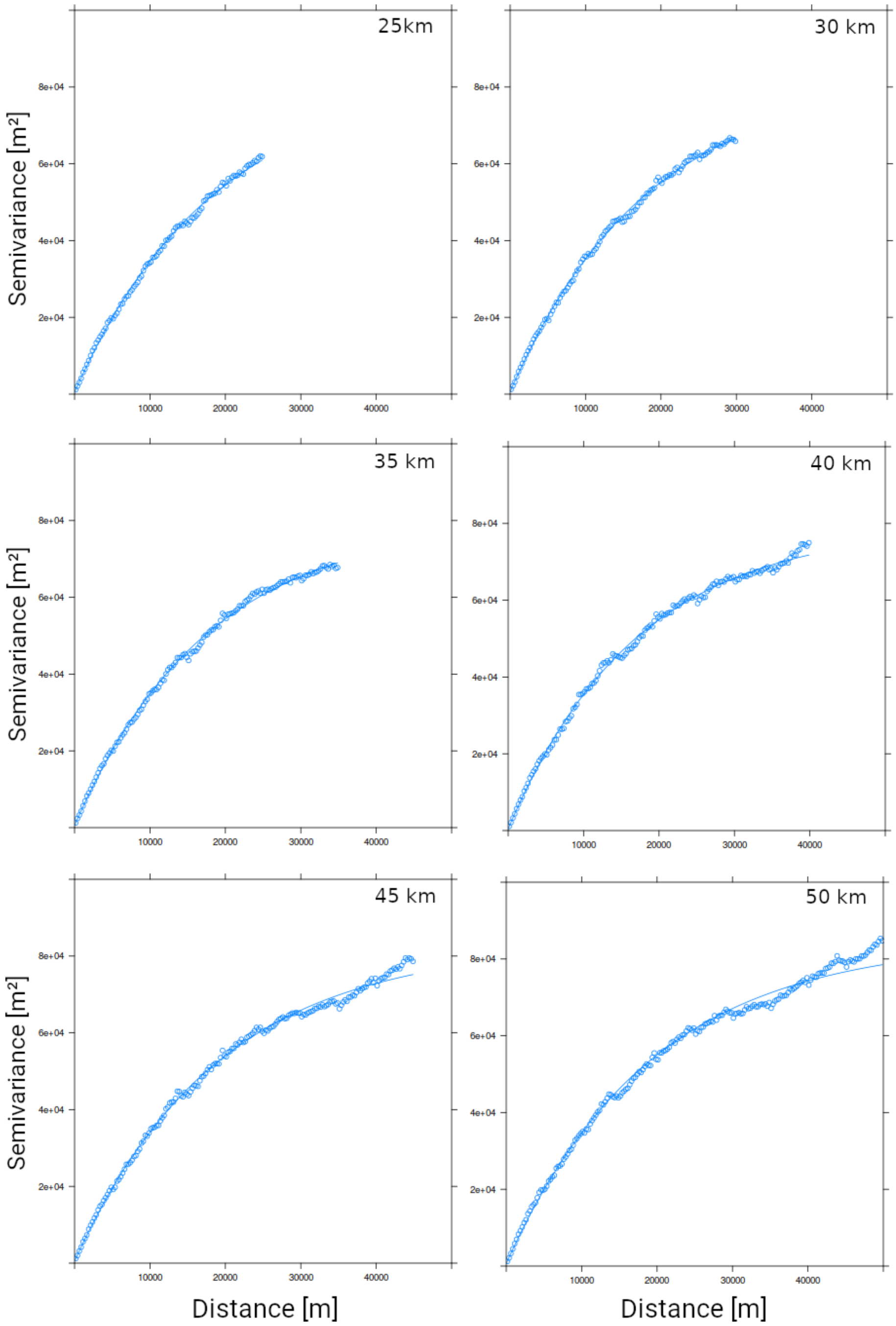

Figure S2. Semivariograms of bedrock topography for Pine Island Glacier from ungridded airborne RES observations described in the main text with exponential least-squared-error fits (lines). Different fitting intervals are used (as quoted in each panel) to investigate the impact of the fitting interval on the parameter values, which are shown in Table S1.

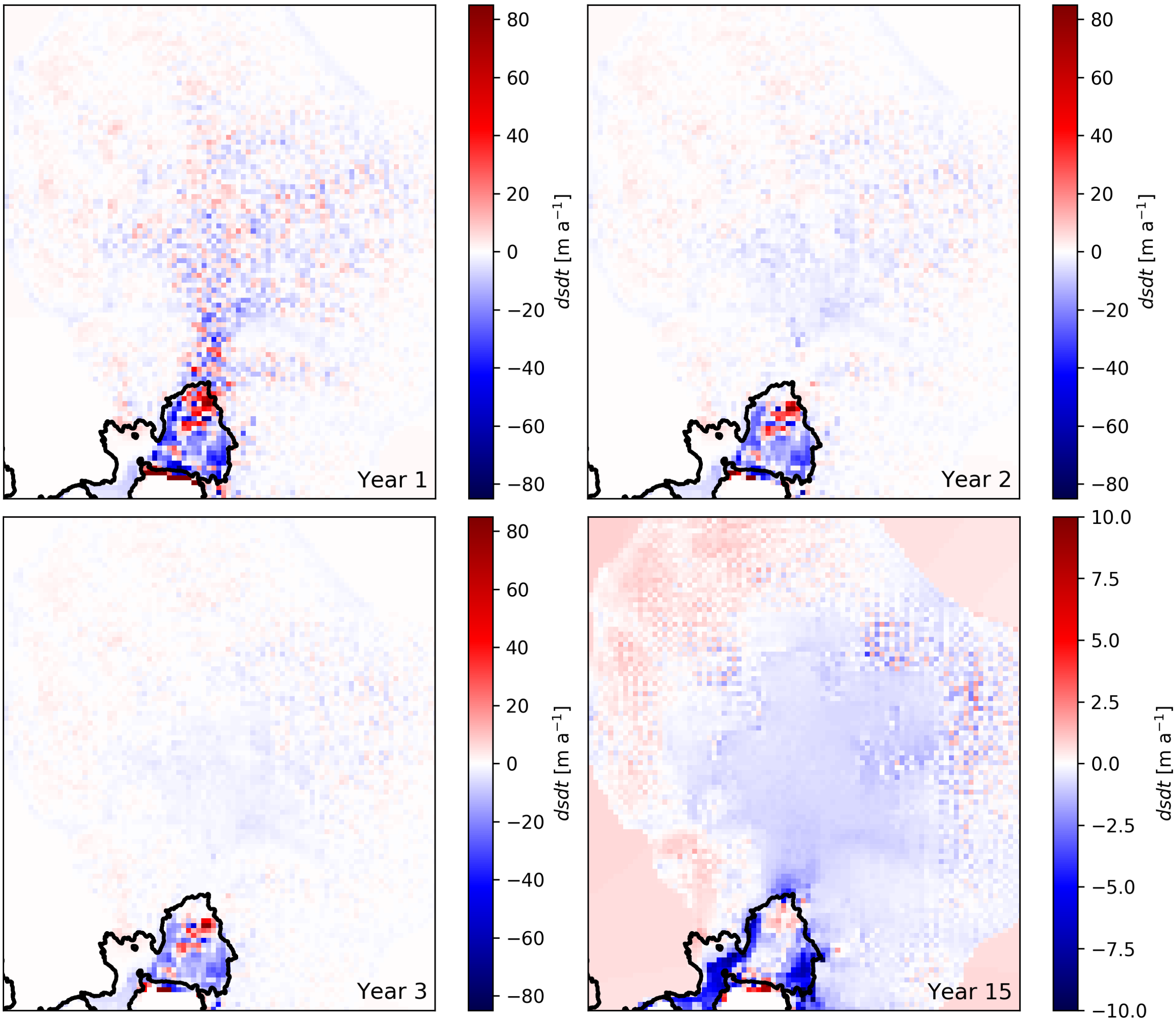

Figure S3. Ice thickness change across PIG model domain in the beginning of the simulations after initializing with velocity data from 1996 to 2016 (years of simulation shown in the lower right corners). Based on a statistically generated topography (B_r #5) with low forcing and plastic friction. Note the smaller colour range in the lower right panel.

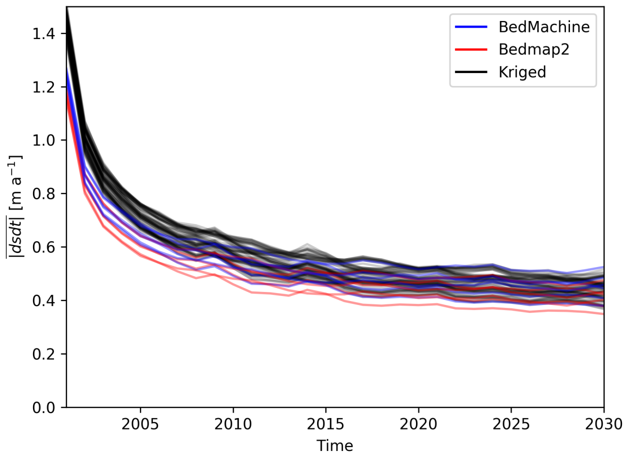

Figure S4. Spatial mean of absolute ice thickness change across PIG model domain for the beginning of the simulations. The initial drop can be associated with BISICLES adjusting to a self-consistent state.

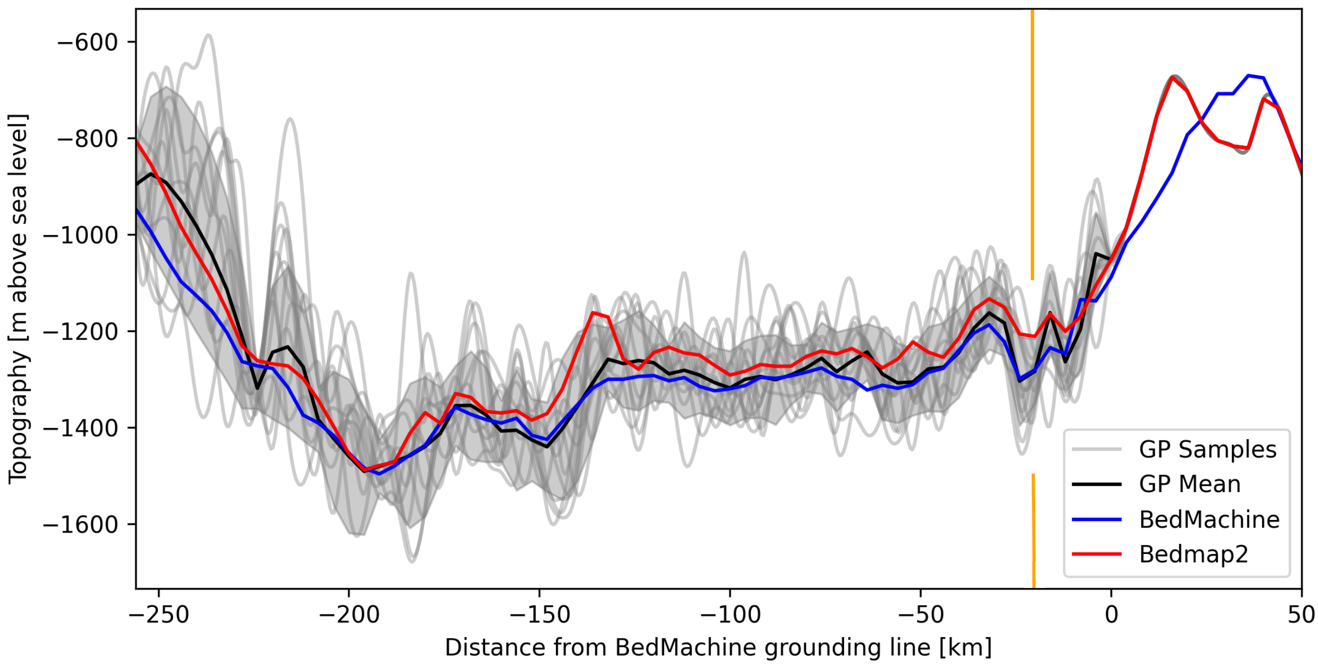

Figure S5. Bedrock topographies on 4 km resolution for Bedmap2, BedMachine, 12 topographies statistically generated here (B_r; for illustration interpolated with a quadratic spline) and the GP model trained on 30 km domain for which shading illustrates $\pm\sigma$. The cross-section roughly follows the center of PIG, as shown in Figure 1 in the main text from point A (left) to point D (right). Grounding line location (x=0) is based on BedMachine geometry which coincides for this section with the extent of the GP models. Under the ice shelf (as defined by Bedmap2) the topographies statistically generated here use the Bedmap2 topography. The orange line highlights a location mentioned in the text.

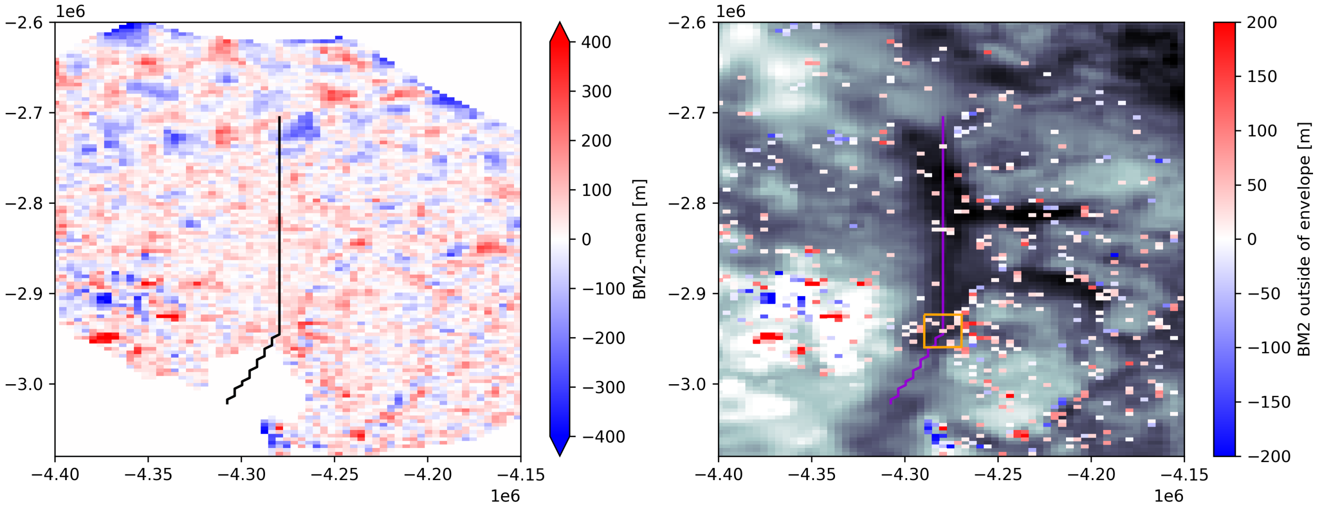

Figure S6. Left: Difference of Bedmap2 and the mean of all statistically generated topographies used here. Right: Difference between Bedmap2 and the closest member of the statistically generated ensemble where Bedmap2 is outside of the envelope of those topographies. At locations where Bedmap2 lies within the range of the statistically generated topographies, the Bedmap2 topography itself is shown (grey shading in background). For comparison, the central flow line of PIG as in Figure 1 in the main text. The orange frame highlights a region mentioned in the text.

6. Additional Supporting Information (Files uploaded separately)

Movie S 0.1. Basal stress parameter τ_b in Pa. Where ice is ungrounded the basal friction is set to zero, otherwise the parameter from the initial model inversion is shown. The animation shows the retreat of the grounded ice by an expansion of zero valued τ_b over 100 years (also highlighted by black line) with Weertman friction law and exponent of $m = 1/8$ and Bedmap2 topography.

Movie S 0.2. as Movie S0.1 but for BedMachine topography.

Movie S 0.3. as Movie S0.1 but for statistically generated topography 'Br001'.

Movie S 0.4. as Movie S0.1 but for statistically generated topography 'Br002'.